A Window-Adaptive Centroiding Method Based on Energy Iteration for Spot Target Localization

Jingyu Bao, Haiyang Zhan, Ting Sun, Sheng Fu, Fei Xing, and Zheng You

***Abstract*— The random noise of complementary metal–oxide–semiconductor (CMOS) image sensor is the main factor limiting the further improvement of high-accuracy spot target detection. Accordingly, a window-adaptive centroiding method based on energy iteration is proposed in this article. The method can effectively mitigate the problem of localization performance fluctuations caused by the random noise at the low-intensity pixels within the extraction window. By analyzing the centroiding error model and the random noise of CMOS detectors, simulations are used to deduce that pixel response random noise that remains after removing systematic errors is the main factor limiting further improvement in positioning accuracy. Based on the generally applicable threshold centroiding algorithm, the influence of the pixel response within the extraction window on the centroiding accuracy is derived according to the pixel energy and the pixel location relative to the target centroid. This leads to an iterative method, which combines the pixels with better performance as a new extraction window and recalculates the target centroid. The effectiveness of the algorithm at the signal-to-noise ratio (SNR) typical for real cases is simulated and analyzed. An experimental scheme is designed for the subpixel movement of point targets with a measurement platform based on a high-precision rotary table and a star tracker to validate our algorithm. Further real star experiment is conducted to verify the effectiveness of the algorithm. The results of the experiments indicate that the proposed method can reduce the random noise effect on spot extraction accuracy.**

***Index Terms*— Localization algorithm, optical instrumentations, optical measurement, space instrumentations.**

I. Introduction

SPOT target optical measurement is the crucial and universal technology for high-precision space navigation [1]–[3], medical fluorescence positioning [4], [5], and microscopy super-resolution imaging [6], [7]. In this article, the main goal is to improve spot target localization. Our study is for star localization using a spatial optical measurement instrument called star tracker but can be generalized to other fields. A description of the satellite attitude measurement application of the star tracker is shown in Fig. 1. When the instrument parameters and the number of measured stars are determined, the centroiding accuracy directly determines the output attitude accuracy of the star tracker. For high-accuracy attitude fixing tasks, more accurate star spot localization method is required.

The conventional centroiding algorithm with threshold is used in the AST series star sensors (Lockheed Martin, Bethesda, MD, USA) [8] and the star sensors of Jena-Optronik (Germany) [9] to calculate the subpixel position of star centroids. Then, the centroid is output by a continuous filtering algorithm to reduce the random noise. However, the filtering method is usually limited by systematic errors and has high computational complexity. The accuracy of this method is about 1/50 pixels and has the potential to be further improved. In 2005, the JPL Laboratory modeled and analyzed the error of star centroiding to conclude that the error of the image detector and the centering system are two important factors affecting the accuracy of the final centroid location [10]. The error of the image detector was reduced by utilizing correction and filtering, and then, the centering system error was eliminated through calibration. Their research points out that the accuracy improvement brought by Gaussian fitting and the numerical fitting algorithm is limited in the actual application of star sensors because it would involve a complex calculation [11]–[13]. Therefore, the centroiding algorithm with threshold value is the most appropriate localization method. Hence, with the improvement of the denoising level of complementary metal–oxide–semiconductor (CMOS) image detectors, it has been widely used in star trackers. We also note the substantial research on the high-precision positioning method of CMOS image detectors, and it has been carried out [14]–[16]. In 2014, a study on threshold algorithm demonstrated that the influence of the noise of image detectors on the variance of centroiding results is related to the threshold selected [17]. The existence of a single threshold on all pixels would cause extra noise to have a greater impact on centroid positioning fluctuations. The traditional threshold algorithm does not discuss the influence of random noise on the centroid determination of spot targets with different energy distributions. Therefore, a single-threshold algorithm cannot achieve further improvement in centroiding accuracy. Consequently, the iterative method has become the focus of research. In 2020, based on studies of Shack–Hartmann wavefront sensors in the field of adaptive optics, Poladyan *et al.* [18] proposed an

Manuscript received November 10, 2021; revised March 29, 2022; accepted April 11, 2022. Date of publication May 13, 2022; date of current version May 19, 2022. This work was supported in part by the National Natural Science Foundation of China under Grant 51827806 and in part by the National Key Research and Development Program of China under Grant 2016YFB0501201. The Associate Editor coordinating the review process was Dr. Shiraz Sohail. *(Corresponding authors: Fei Xing; Zheng You.)*

Jingyu Bao, Haiyang Zhan, Sheng Fu, Fei Xing, and Zheng You are with the Beijing Advanced Innovation Center for Integrated Circuits, Department of Precision Instrument, and the State Key Laboratory of Precision Measurement Technology and Instruments, Tsinghua University, Beijing 100084, China (e-mail: bao-jy14@mails.tsinghua.edu.cn; hbyszhy@163.com; fs17@mails.tsinghua. edu.cn; xingfei@mail.tsinghua.edu.cn; yz-dpi@mail.tsinghua.edu.cn).

Ting Sun is with the Joint International Research Laboratory of Advanced Photonics and Electronics, Beijing Information Science and Technology University, Beijing 100192, China (e-mail: sunting@bistu.edu.cn).

Digital Object Identifier 10.1109/TIM.2022.3169757

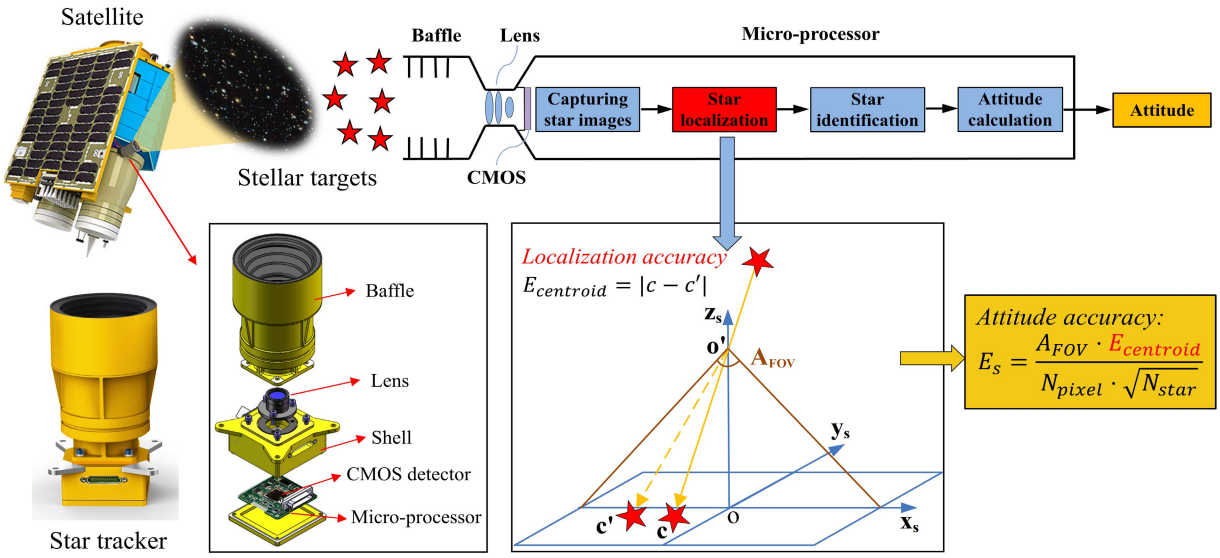

Fig. 1. High-accuracy spot target localization for satellite attitude measurement applications.

iterative weighted centroid algorithm (IWCOG) to make the centroiding accuracy better than 1/100 pixels. Their method maximized the output centering result of the cross correlation function between the tracking topography of discrete sampling and the actual star-point topography by iterating the centroid of the tracking target image. In relative terms, the IWCOG algorithm should be the algorithm with the highest centering accuracy [19]–[22]. However, Thomas *et al.* [23] found that when the signal-to-noise ratio (SNR) did not meet the tracking conditions, the cross correlation function could not seek the optimal solution, and the tracking spot target morphology was greatly affected by random noise. In 2021, Sun *et al.* [24] proposed a filtered centering method based on the motion pattern, which can effectively solve the problem of random noise. However, this algorithm requires continuous motion information of the point target and is not real time [25]. Therefore, to deal with the influence of random noise caused by CMOS image detector response during centroiding, this article proposes an energy iteration-based window-adaptive centroiding algorithm (EIWA). The basic principle of this algorithm is shown in Fig. 2. It shows the effect of CMOS random noise fluctuations on position accuracy in a spot target energy distribution. To obtain a more stable centroiding accuracy, the applicable centroid calculation windows are iterated for spot targets with different energy distribution forms. We then analyze whether each pixel should be included in the extraction window and utilized in the calculation according to its influence on the centroiding accuracy. Compared with other algorithms, the proposed EIWA algorithm has the following advantages.

1) The spot target energy distribution information does not need to be known before calculating which is a more general approach. The Gaussian surface fitting method requires knowledge of the model function [26], [27]. The centroiding accuracy of this type of algorithm is related to the model accuracy.
2) The algorithm can adaptively reduce the impact of CMOS random noise through energy analysis. Random centroiding error fluctuations due to overfiltering and weighting can be avoided. Other methods will introduce the corresponding systematic error of weighting and the fitted model. Systematic errors generated by using the EIWA algorithm are more easily corrected.
3) Low algorithm complexity and enabling real-time applications. In contrast to other numerical iterative algorithms, this algorithm is based on the traditional centroiding method of iteration. The number of iterations and process time is much lower than the IWCOG algorithm [28], [29]. Also, combined with the hardware centroiding module, it can realize the practical application of the star tracker. Although other high-accuracy algorithms can achieve better centroiding accuracy, currently, most of them can only be simulated in the laboratory, such as IWCOG's wavefront prediction and deep learning methods [30].

II. Analysis of Subpixel Centroiding Error

In this section, errors of spot target imaging and localization are analyzed for the iterative algorithm. Spot target can be positioned at the subpixel level through defocus imaging processing and image detector sampling. In the ideal case, the intensity distribution of the point target can be expressed by a 2-D Gaussian function as

$$I(x, y) = \frac{I_0}{2\pi\sigma^2} \exp\left(-\frac{(x - x_0)^2 + (y - y_0)^2}{2\sigma^2}\right). \quad (1)$$

I_0 is the total energy of the spot target on the detector, x_0 and x_0 are the real spot center, and σ is the Gaussian radius relevant to optical system design. Since x and y are symmetric, just the analysis of the x-direction can be carried out. The analysis for the y-direction will be identical.

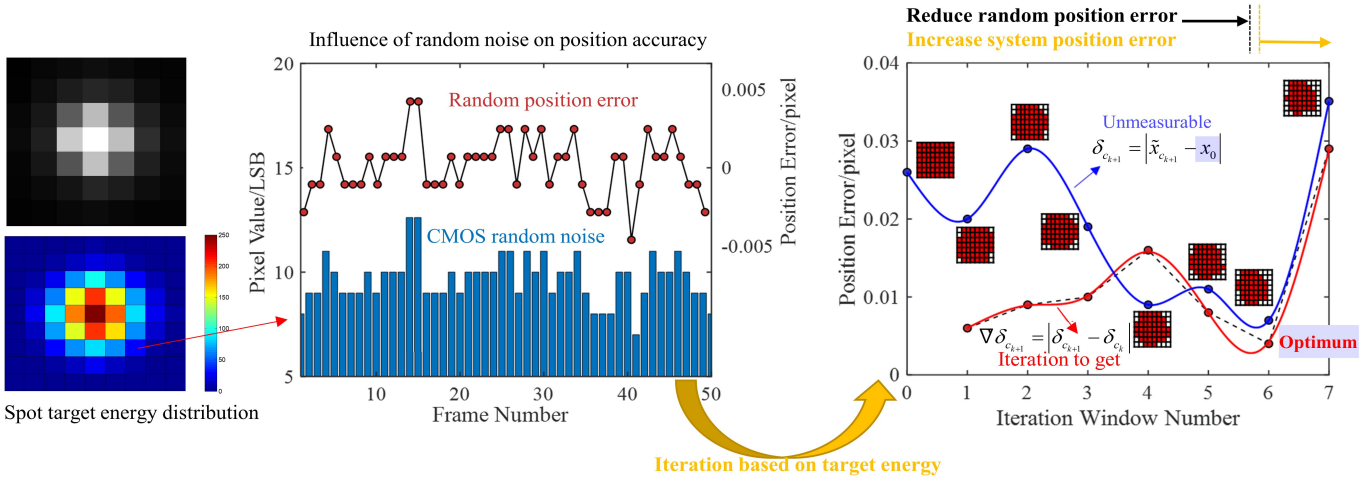

Fig. 2. Schematic of window-adaptive method based on the energy iteration algorithm.

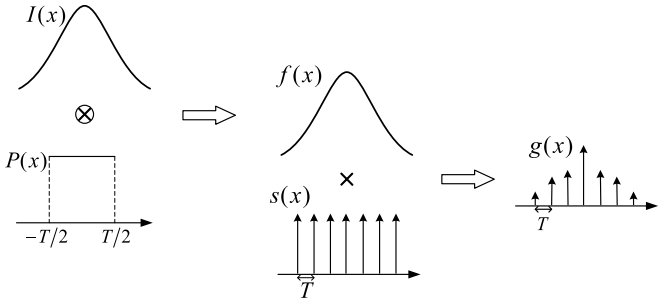

Fig. 3. Imaging process of the spot target on the CMOS detector.

The imaging process of the spot target on the image detector is shown in Fig. 3. The continuous spot energy point diffusion PSF function $I(x)$ convolves with the pixel response function $P(x)$ of the image detector to obtain the continuous energy function $f(x)$ received by the pixel. Then, discrete multipixels $s(x)$ sample $f(x)$ to get the window pixel sampling function $g(x)$. Here, $p(x)$ is the door function and $s(x)$ is the comb function [31].

Through optical discrete processing, the spot target that will light intensity distribution on the connecting several detectors' pixels is sample output. With the spot target energy distribution function $I(x)$ and image detector pixel response function $P(x)$, the convolution function is defined as

$$f(x) = I(x) \otimes P(x). \tag{2}$$

The actual centroid of the star is fixed using the corresponding point spread function $I(x, x_0)$. The entire discrete sampling process of the star can be expressed as

$$g(x) = [I(x, x_0) \otimes P(x)] \times s(x) \tag{3}$$

where $g(x)$ is the detector response calculated for the actual measurement, which is directed against the point spread function $I(x, x_0)$'s effective PSF function (ePSF, effective PSF) [32], [33].

At present, the centroid of the gray method (CG) is commonly used to calculate the centroid of the discrete point targets. The calculation formula for ideal spot target centroid $\bar{x}_0$ without image noise can be represented as

$$\bar{x}_0 = \frac{\sum_W^{x_k g_k}}{\sum_W^{g_k}} \tag{4}$$

where x_k is the number k center coordinates of centroid extraction the region, g_k is the ideal response of the k pixel, and W is the calculated window.

However, the actual detector response i_k with noise for spot target centroid $\tilde{x}_c$ is

$$\tilde{x}_c = \frac{\sum_W^{x_k i_k}}{\sum_W^{i_k}}. \tag{5}$$

The actual detector response i_k contains detector random noise σ_{i_k} and n_{i_k}, which is the pixel noise of the single measurement. The spot target ideal energy response is g_k

$$i_k = g_k + n_{i_k}. \tag{6}$$

The centroid error caused by CMOS random noise is δ_i, which can be determined as

$$\delta_i = \sum_W \left(\frac{\partial \tilde{x}_c}{\partial i_k} \right) \times n_{i_k}. \tag{7}$$

Next, the derivative of $\tilde{x}_c$ from (5) can be obtained as

$$\frac{\partial \tilde{x}_c}{\partial i_k} = \frac{x_k \sum_W i_k - \sum_W x_k i_k}{\left(\sum_W i_k\right)^2} = \frac{x_k - \tilde{x}_c}{\sum_W i_k}. \tag{8}$$

Now, (7) can be expressed as

$$\delta_i = \sum_W \left(\frac{x_k - \tilde{x}_c}{\sum_W i_k} \right) \times n_{i_k}. \tag{9}$$

$\bar{x}_0$ is the center of the centroid, which is calculated by the discrete CG method without detector response noise. δ_i is random noise caused by the CMOS detector. For this error model, we discuss in Section II-B.

A. Systematic Error Modeling and Analysis of Centroid Gravity Algorithm

For the real centroid x_0, one should continuously compute the spot target energy distribution as

$$x_0 = \frac{\iint_{\mathrm{ROI}} x f(x) dx}{\iint_{\mathrm{ROI}} f(x) dx}. \tag{10}$$

When discrete pixel centers are used instead of continuous energy centers, systematic errors will occur as [34]–[36]

$$\bar{x}_0 = \frac{\sum_{k=1}^{n} x_k g_k}{\sum_{k=1}^{n} g_k} = \frac{\int_{-\infty}^{\infty} x g(x) dx}{\int_{-\infty}^{\infty} g(x) dx}. \tag{11}$$

The Fourier transform of $g(x)$ can be represented as

$$G(w) = \int_{-\infty}^{\infty} g(x) e^{-2\pi j x w} dx \tag{12}$$

then

$$\int_{-\infty}^{\infty} g(x) dx = \int_{-\infty}^{\infty} g(x) e^{-2\pi j x w} dx|_{w=0} = G(0) \tag{13}$$

the derivative of $G'(w)$ can be given as

$$\begin{aligned} G'(w) &= \frac{dG(w)}{dw} = \int_{\infty}^{\infty} (-2\pi j x) \times g(x) e^{-2\pi j x w} dx \\ &= -2\pi j \int_{\infty}^{\infty} x g(x) e^{-2\pi j x w} dx. \end{aligned} \tag{14}$$

Based on (14), $G'(0) = -2\pi j \int_{-\infty}^{\infty} x g(x) dx$ and $\int_{-\infty}^{\infty} x g(x) dx = -G'(0)/2\pi j$.

From (14), (13) can be written as

$$\bar{x}_0 = \frac{\sum_{k=1}^{n} x_k g_k}{\sum_{k=1}^{n} g_k} = \frac{\int_{-\infty}^{\infty} x g(x) dx}{\int_{-\infty}^{\infty} g(x) dx} = -\frac{G'(0)}{2\pi j G(0)}. \tag{15}$$

The energy function of the center at the origin is defined as $f_e(x)$, and for real spot target center x_0, it can be given as

$$f(x) = f_e(x - x_0). \tag{16}$$

Due to the frequency-domain shift theorem, the frequency domain can be expressed as

$$F(w) = \exp(-2\pi j x_0 w) F_e(w). \tag{17}$$

According to the imaging process analysis (3), the conversion to the frequency domain can be given as

$$G(w) = F(w) \otimes S(w) = \exp(-2\pi j x_0 w) \times F_e(w) \otimes S(w) \tag{18}$$

where $S(w)$ is the frequency-domain transform about discrete multipixel samples function $s(x)$.

Then

$$\begin{aligned} G'(w) &= F'(w) \otimes S(w) \\ &= \big[-2\pi j x_0 \exp(-2\pi j x_0 w) F_e(w) \\ &\quad + \exp(-2\pi j x_0 w) \times F_e'(w)\big] \otimes S(w). \end{aligned} \tag{19}$$

Let (17)–(19) get into (15)

$$\begin{aligned} \bar{x}_0 &= -\frac{G'(0)}{2\pi j G(0)} \\ &= \frac{\big[-2\pi j x_0 \exp(-2\pi j x_0 w) F_e(w) + \exp(-2\pi j x_0 w) F_e'(w)\big] \otimes S(w)}{-2\pi j \exp(-2\pi j x_0 w) F_e(w) \otimes S(w)}\Bigg|_{w=0} \\ &\quad \frac{-2\pi j \exp(-2\pi j x_0 w) F_e(w) \otimes S(w)}{} \end{aligned} \tag{20}$$

and

$$\bar{x}_0 = x_0 - \frac{\exp(-2\pi j x_0 w) F_e'(w) \otimes S(w)}{2\pi j \exp(-2\pi j x_0 w) F_e(w) \otimes S(w)}\Bigg|_{w=0}. \tag{21}$$

The frequency-domain variation of sampling function is the comb tooth function $S(w) = \sum_{n=-\infty}^{n=+\infty} \delta(w - n/T)$ and the convolution can be given as

$$\begin{aligned} \varepsilon_s &= \bar{x}_0 - x_0 \\ &= -\frac{1}{2\pi j} \frac{\sum_{n=-\infty}^{n=+\infty} \left\{\exp\left[-2\pi j x_0 \left(w - \frac{n}{T}\right)\right] F_e'\left(w - \frac{n}{T}\right)\right\}}{\sum_{n=-\infty}^{n=+\infty} \left\{\exp\left[-2\pi j x_0 \left(w - \frac{n}{T}\right)\right] F_e\left(w - \frac{n}{T}\right)\right\}}\Bigg|_{w=0} \\ &= -\frac{1}{2\pi j} \frac{\sum_{n=-\infty}^{n=+\infty} \left[\exp\left(2\pi j x_0 \frac{n}{T}\right) F_e'\left(-\frac{n}{T}\right)\right]}{\sum_{n=-\infty}^{n=+\infty} \left[\exp\left(2\pi j x_0 \frac{n}{T}\right) F_e\left(-\frac{n}{T}\right)\right]}. \end{aligned} \tag{22}$$

Equation (22) can be simplified as

$$\varepsilon_s = \frac{1}{\pi} \frac{\sum_{n=1}^{n=+\infty} F_e'\left(\frac{n}{T}\right) \sin\left(2\pi x_0 \frac{n}{T}\right)}{F_e(0) + 2\sum_{n=1}^{n=+\infty} F_e\left(\frac{n}{T}\right) \cos\left(2\pi x_0 \frac{n}{T}\right)}. \tag{23}$$

According to the imaging process, $F_e(w)$ can be given as

$$F_e(w) = I(w, 0) \times P(w). \tag{24}$$

Then, using $I(w, x_0) = I_0 \exp[-2(\pi\sigma w)^2] \exp(-j2\pi w x_0)$ and $P(w) = \sin(T\pi w)/(T\pi w)$, it can be obtained as

$$F_e(w) = I_0 \exp\left[-2(\pi\sigma w)^2\right] \times \frac{\sin(T\pi w)}{T\pi w}. \tag{25}$$

According to (25) and $F_e(0) = I_0$, $F_e(n/T) = 0 (n \neq 0)$.

Hence, (25) can be given as

$$\varepsilon_s = \frac{1}{\pi} \frac{\sum_{n=1}^{n=+\infty} F_e'\left(\frac{n}{T}\right) \sin\left(2\pi x_0 \frac{n}{T}\right)}{I_0} \tag{26}$$

where $F_e'(n/T) = (-1)^n I_0 \exp[-2(\pi\sigma(n/T))^2] \times n/T$.

Finally, the error model can be obtained as

$$\varepsilon_s = \frac{T}{\pi} \sum_{n=1}^{n=+\infty} (-1)^n \exp\left[-2\left(\pi\sigma\frac{n}{T}\right)^2\right] \sin\left(2\pi x_0 \frac{n}{T}\right) \times \frac{1}{n}. \tag{27}$$

Pixel length T can be a unified unit as

$$\varepsilon_s = \frac{1}{\pi} \sum_{n=1}^{n=+\infty} (-1)^n \exp\left[-2(\pi\sigma n)^2\right] \sin(2\pi x_0 n) \times \frac{1}{n}. \tag{28}$$

According to the systematic error formula (28), the error model expression does not contain the item of I_0. Thus, the energy of the target at the point of incidence does not affect the S-curve error. The previous two terms are the main error terms. With different Gaussian radius distributions, they can be simulated and can be compared with the theoretical physical meaning, as shown in Fig. 4(a)–(d). We make the ideal spot target's center x_0 continuously located in the pixel position [0 1]. Then, the conversion from continuous energy function to discrete sampling is performed. The spot target centroid $\bar{x}_0$ is calculated by the discrete CG method. The error

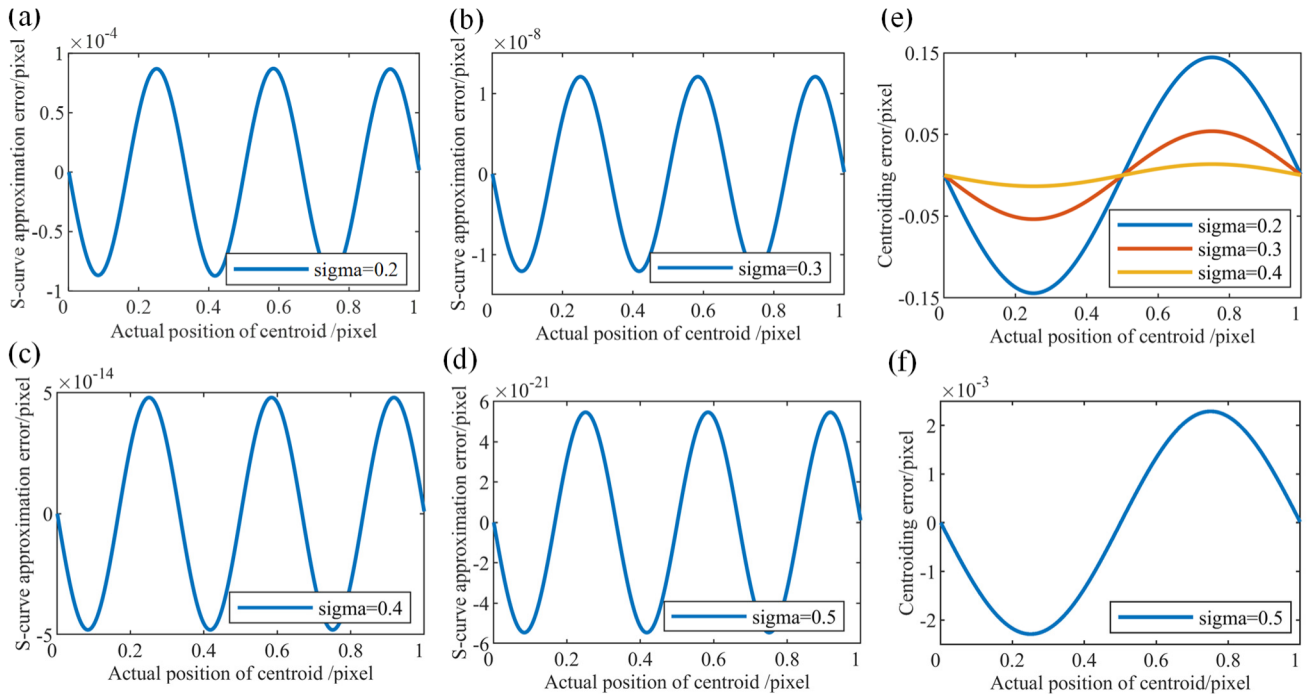

Fig. 4. (a)–(d) S-curve approximation error obtained by energy representation simulation and (e) and (f) simulation curve of centroiding system error S-curve error model.

profiles of spot targets with different phases in pixel can be calculated.

Therefore, it can be seen from the approximate error curve that the error function can be approximated to the previous two main terms. When the radius of the Gaussian σ is within 0.5–0.2, the approximate error is less than 0.0001 pixel. Therefore, the centroiding system error can be approximately expressed as

$$\varepsilon_s \approx \frac{1}{\pi}\left\{ -\exp\left[-2(\pi\sigma)^2\right] \times \sin(2\pi x_0) + \exp\left[-8(\pi\sigma)^2\right] \times \sin(4\pi x_0) \times \frac{1}{2}\right\}. \quad (29)$$

Then, according to (5), (9), and (29), the error between the actual discrete CG method and the real center of spot target can be obtained as

$$\tilde{x}_c = \bar{x}_0 + \delta_i = \varepsilon_s + x_0 + \delta_i. \quad (30)$$

The final expression for the systematic error can be given as

$$\delta_{\tilde{x}_c} = \tilde{x}_c - x_0 = \varepsilon_s + \delta_i \quad (31)$$

where $\delta_i = \sum_W ((x_k - \tilde{x}_c / \sum_W i_k)) \times n_{i_k}$.

According to (31), the system error of centroiding can be divided into two parts.

1) The centroiding error ε_s caused by a continuous energy center. This is replaced by the geometric center in discrete sampling with a period of pixels presented as an S-curve as shown in Fig. 4.
2) The imaging detector error δ_i caused by detector response noise with spatial differences between pixels and related to the distance from the center of the spot center.

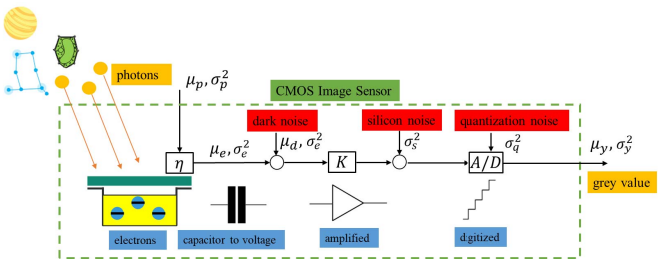

Fig. 5. Spot target imaging on the image detector imaging diagram.

The principle of centroiding system error helps analyze the final noise of each part. The effect of random noise is the main focus of this article. Therefore, the noise analysis of the image detector is crucial for overall error analysis. Simulation analysis and discussion are carried out in the following parts.

B. CMOS Imager Noise of Centroiding Error

The imaging process of spot target on the CMOS image detector is shown in Fig. 5. The signal photons μ_p reach the detector after quantum conversion (with conversion efficiency, η) into electrons stored in the capacitive structure. After the quantum transformation, the variable is μ_e. At this time, the signal is superimposed with the dark current noise μ_d caused by the circuit structure and then amplified with gain K, and finally, the digital gray signal output μ_y is obtained by A/D conversion. Random noise σ_s and quantization noise σ_q caused by silicon structure exist in the process of analog amplification [37]–[39].

The whole process of imaging output gray value can be given as

$$\mu_y = K(\mu_e + \mu_d). \tag{32}$$

According to the imaging process, the detector noise can be obtained as

$$\sigma_y^2 = K^2\sigma_e^2 + K^2\sigma_d^2 + \sigma_s^2 + \sigma_q^2. \tag{33}$$

The photon shot noise $\sigma_e^2 = \mu_e$ and dark current shot noise $\sigma_d^2 = \mu_d$ are Poisson distributions. Now, (33) can be given as

$$\begin{aligned}\sigma_y^2 &= K^2\sigma_d^2 + K^2\mu_e + \sigma_s^2 + \sigma_q^2 \\ &= K^2\sigma_d^2 + K\left(\mu_y - \mu_{y,\text{dark}}\right) + \sigma_s^2 + \sigma_q^2.\end{aligned} \tag{34}$$

With $\mu_{y,\text{dark}} = K\mu_d$, let $\mu_{y'} = \mu_y - \mu_{y,\text{dark}}$. The output gray value is subtracted from the dark current value to obtain the output gray noise expression

$$\sigma_{y'}^2 = K\mu_{y'} + \sigma_s^2 + \sigma_q^2. \tag{35}$$

The random noise σ_s caused by the silicon structure, which is different from CCD detectors, with each pixel having a different amplification structure. Hence, σ_s has the spatial difference. Spatial nonuniform noise can be eliminated by calibration, and random noise is the main cause of fluctuations in the centroiding process. However, quantization noise can cause the limited random noise, the photon shot noise, and the Gaussian random noise caused by the input signal that are analyzed in this article

$$\sigma_{i_k}^2 = K\mu_{i_k'} + \sigma_s^2 \tag{36}$$

where σ_{i_k} is the noise variance corresponding to the pixel response i_k and $\mu_{i_k'} = \mu_{i_k} - \mu_{i_k,\text{dark}}$.

For single-frame star map, Poisson noise that varies with light intensity is the main noise item affecting the SNR of star imaging. The centroid location measured is affected by imaging noise, which will drown the S-curve error existing in the gray algorithm and cannot be measured. Therefore, there is no way to compensate for it. In addition, although the random noise level of the detector is low, the pixel farther away from the centroid also has a great influence on the centering result, which needs to be discussed.

The energy-dependent Poisson noise $\sigma_{e_k}^2$ caused by the detector response is added to the spot target with the Gaussian radius of 0.3 and 1 least significant bit (LSB) random a Gaussian noise σ_s^2, and the response noise can be given as

$$\sigma_{i_k}^2 = \sigma_{e_k}^2 + \sigma_{s_k}^2 = \mu_{i_k} + \sigma_{s_k}^2. \tag{37}$$

Based on this distribution and (9), the centroid positioning error of a single frame is simulated, as shown in Fig. 6 [CMOS image sensor (CIS)]. It can be seen from the simulation curve that the measurement of a single frame is seriously affected by random noise. If the spot target SNR is low, the random centroiding error will be large, resulting in systematic S-curve errors that cannot be effectively observed and measured.

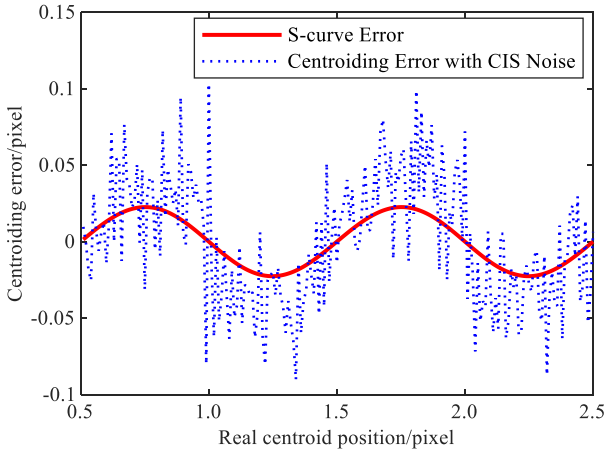

Fig. 6. Simulation of single frame centroiding error ($\sigma = 0.3$).

III. Window-Adaptive Centroiding Method Based on Energy Iteration

The window-adaptive centroiding method based on energy iteration is proposed in this section. The basic iterative principle is based on the previously proposed centroiding error model. The iterative loss function and variable window condition are also formulated.

A. Principle of EIWA Method

Based on the noise source analysis in the previous section, we now propose an adaptive window centroiding based on energy iteration. The flow diagram of the algorithm is shown in Fig. 7.

According to the analysis in the previous section, preliminary research conclusions can be obtained that the presence of random noise can affect the measurement of S-curve errors. The S-curve systematic error is also difficult to determine whether the influence of random noise is not reduced. In particular, pixels at the edge of the extracted window whose noise variance fluctuates have a large impact on the final centroid localization. Therefore, the grayscale response of the pixels in the window needs to be analyzed at each calculation of the centroid to determine whether they need to be involved in the calculation. In the process of changing the window, the centroiding error will change. Accordingly, a window iteration method is proposed to obtain the convergent change curve of the centroid error from large to small, where the local optimal window can be calculated by continuous iteration. The main steps of the resulting algorithm are given as follows.

1) Iterate the centroid loss function: let the error δ_c between the final output center and the ideal center be minimized, which can be given as

$$L\left(\delta_{c(W_n)}\right) = |\tilde{x}_{c_n} - x_0| = |\varepsilon_{s_n} + \delta_{i_n}| \tag{38}$$

where W_n is the nth iteration centroid window, the initial iteration window is W_0, and the iteration termination error is $\varepsilon = 0.005$ pixel.

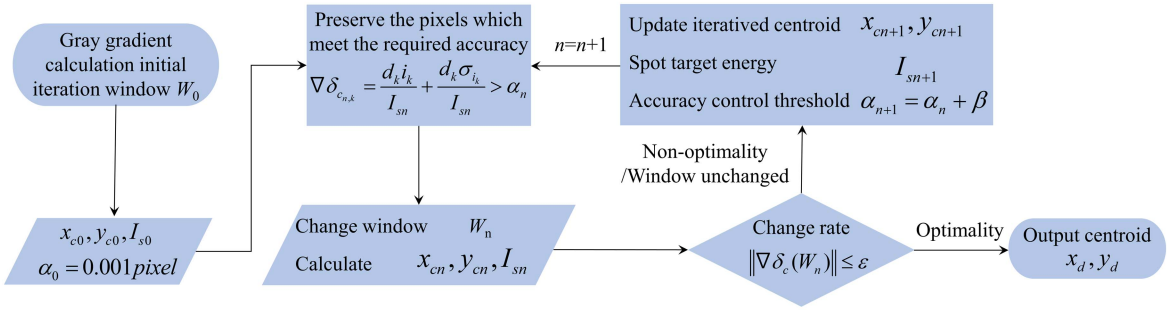

Fig. 7. Flowchart of window-adaptive centroiding method based on energy iteration.

2) Calculate the difference between the two iteration loss functions

$$\nabla\delta_c = \delta_{c(W_n)} - \delta_{c(W_{n-1})}. \tag{39}$$

3) When $\|\nabla\delta_{c(W_n)}\| \le \varepsilon$, the iteration is finished. Then, the centroid calculation is carried out using W_n final iterative window. At this point, the loss function is locally minimized

$$L\left(\delta_{c(W_n)}\right) = \min|\tilde{x}_{c_n} - x_0|. \tag{40}$$

B. Iterative Model Analysis

In the process of window change, the centroid of two measurements can be shown to be

$$\tilde{x}_{c_n} = \frac{\sum_{W_n} x_k i_k}{\sum_{W_n} i_k}, \quad \tilde{x}_{c_{n+1}} = \frac{\sum_{W_{n+1}} x_k i_k}{\sum_{W_{n+1}} i_k}. \tag{41}$$

The two changed windows of pixels will be reduced. According to the error model (31), the systemic error can be obtained as

$$\begin{aligned}\nabla\varepsilon_{c_{n+1}} &= \varepsilon_{c_{n+1}} - \varepsilon_{c_n} = \bar{x}_{0_{n+1}} - x_0 - \left(\bar{x}_{0_n} - x_0\right) \\ &= \bar{x}_{0_{n+1}} - \bar{x}_{0_n} = \frac{\sum_{W_{n+1}} x_k g_k}{\sum_{W_{n+1}} g_k} - \frac{\sum_{W_n} x_k g_k}{\sum_{W_n} g_k}.\end{aligned} \tag{42}$$

According to the window iteration process of EIWA algorithm, as the number of iterations increases, the number of pixels involved in the calculation is reduced. This part of the reduced pixel area we define as ΔW_n

$$\begin{aligned}\nabla\varepsilon_{c_{n+1}} &= \varepsilon_{c_{n+1}} - \varepsilon_{c_n} \\ &= \frac{\sum_{W_{n+1}} x_k g_k}{\sum_{W_{n+1}} g_k} - \frac{\sum_{W_{n+1}} x_k g_k + \sum_{\Delta W_n} x_k g_k}{\sum_{W_{n+1}} g_k + \sum_{\Delta W_n} g_k} \\ &= \frac{\sum_{\Delta W_n} \left(\bar{x}_{0_{n+1}} - x_k\right) g_k}{\sum_{W_n} g_k}.\end{aligned} \tag{43}$$

For the window iteration process, from (9), the random error enhancement is expressed as

$$\begin{aligned}\nabla\delta_{i_{n+1}} &= \delta_{i_{n+1}} - \delta_{i_n} = \frac{\sum_{W_{n+1}} \left(x_k - \tilde{x}_{c_{n+1}}\right) n_{i_k}}{\sum_{W_{n+1}} i_k} \\ &\quad - \frac{\sum_{W_n} \left(x_k - \tilde{x}_{c_n}\right) n_{i_k}}{\sum_{W_n} i_k} \\ &= \frac{\sum_{W_{n+1}} \left(x_k - \tilde{x}_{c_{n+1}}\right) n_{i_k}}{\sum_{W_{n+1}} i_k} \\ &\quad - \frac{\sum_{W_{n+1}} \left(x_k - \tilde{x}_{c_n}\right) n_{i_k} + \sum_{\Delta W_n} \left(x_k - \tilde{x}_{c_n}\right) n_{i_k}}{\sum_{W_{n+1}} i_k + \sum_{\Delta W_n} i_k} \\ &\approx \frac{\sum_{\Delta W_n} \left(\tilde{x}_{c_n} - x_k\right) n_{i_k}}{\sum_{W_n} i_k}.\end{aligned} \tag{44}$$

According to (31), it can be concluded that the centering error is composed of system error and gray noise error. Then, the difference between the two measurements of the centroid can be obtained as

$$\begin{aligned}\nabla\delta_{c_{n+1}} \approx \nabla\varepsilon_{c_{n+1}} + \nabla\delta_{i_{n+1}} &= \frac{\sum_{\Delta W_n} \left(\bar{x}_{0_{n+1}} - x_k\right) g_k}{\sum_{W_n} g_k} \\ &\quad + \frac{\sum_{\Delta W_n} \left(\tilde{x}_{c_{n+1}} - x_k\right) n_{i_k}}{\sum_{W_n} i_k}.\end{aligned} \tag{45}$$

Let $d_k = \tilde{x}_{c_{n+1}} - x_k \approx \tilde{x}_{c_n} - x_k \approx \bar{x}_{0_{n+1}} - x_k$. Since the pixel ideal response g_k and centroid $\bar{x}_{0_{n+1}}$ cannot be obtained, the actual measurements i_k and $\tilde{x}_{c_{n+1}}$ can be approximated as

$$\nabla\delta_{c_{n+1}} \approx \frac{\sum_{\Delta W_n} d_k i_k}{\sum_{W_{n+1}} i_k} + \frac{\sum_{\Delta W_n} d_k n_{i_k}}{\sum_{W_{n+1}} i_k}. \tag{46}$$

1) Discussion of approximate rationality, since the spot target's total energy is SNR = 30 or above (the total energy of the experimental spot target in this article is 2000 LSB), the approximate error magnitude of d_k is 10^{-2}. The denominator is the total energy 10^3 and n_{i_k} is 10. Hence, the approximate error magnitude of the approximate is 10^{-4}. Hence, it is reasonable to use this approximation.
2) Approximation of pixel response noise $n_{i_k} \approx \sigma_{i_k} = (i_k/K)^{1/2}$, it can be got from part 2 of this article. The pixel position that affects the centering is at the edge of the star point with low energy, and the estimated variance of its single measurement can be used to characterize the degree of its influence with a large probability.

According to the accuracy model in the overall window region, the accuracy influence model of a single pixel in the centering region is defined as

$$\nabla\delta_{c_{n+1,k}} \approx \frac{d_k i_k}{I_{s_{n+1}}} + \frac{d_k \sigma_{i_k}}{I_{s_{n+1}}} \tag{47}$$

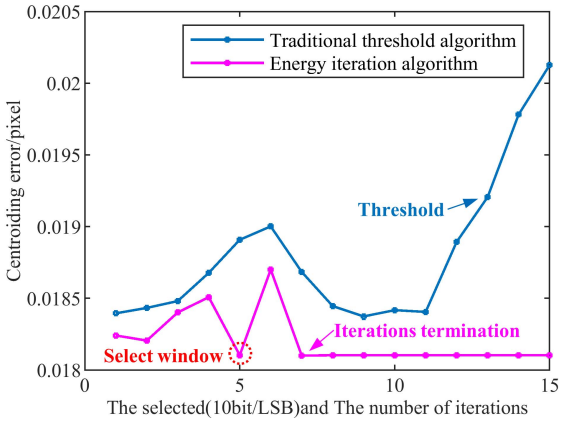

Fig. 8. Comparison of iterative algorithm and traditional threshold algorithm in the Monte Carlo simulation and optimal iterative window position selection process.

where $I_{s_{n+1}} = \sum_{W_{n+1}} i_k$ is the $n+1$ window's total energy.

The centroid pixel energy involved in the calculation of the new window needs to meet the condition

$$\nabla\delta_{c_{n+1,k}} \approx \frac{d_k i_k}{I_{s_{n+1}}} + \frac{d_k \sigma_{i_k}}{I_{s_{n+1}}} > \alpha_{n+1}. \tag{48}$$

Equation (48) determines whether the contribution of the nth pixel position in the extraction window to the centroid change rate meets the threshold value α_{n+1}. The accuracy control threshold for each window iteration is $\alpha_{n+1} = \alpha_n + \beta$. Here, β is the accuracy control step parameter (which can be set to be 0.0005 pixels). For each window change, the threshold is adjusted.

C. Monte Carlo Simulation of EIWA Method

By adding Poisson noise to a star with a Gaussian radius of 0.3, Monte Carlo simulation results using this precision control method are compared with the traditional threshold method. The process of selecting the optimal control threshold and centroid output is shown in Fig. 8.

Thousand Monte Carlo simulations are performed with multiple points and compared with the threshold algorithm. Here, the threshold 6 is selected since it is more stable for this SNR and distribution. This threshold choice is consistent with the later experimental choices.

Through Monte Carlo simulations, the average positioning root-mean-square (rms) of the proposed energy iteration algorithm is seen to be 0.0094 pixels, while the average positioning rms of the traditional threshold algorithm is 0.0142 pixels, which is 0.0048 pixels (33.9%) higher, as shown in Fig. 9.

The calculation window obtained by iteration can be given as ROI′. One can then recalculate the output's final iteration centroid x_d, y_d. With this approach, the centroid of the measured position of subpixels with continuous movements within a pixel is calculated as

$$\tilde{x}_c = \frac{\sum_{(x,y)\in \mathrm{ROI}'} x i(x,y)}{\sum_{(x,y)\in \mathrm{ROI}'} i(x,y)}, \quad \tilde{y}_c = \frac{\sum_{(x,y)\in \mathrm{ROI}'} y i(x,y)}{\sum_{(x,y)\in \mathrm{ROI}'} i(x,y)}. \tag{49}$$

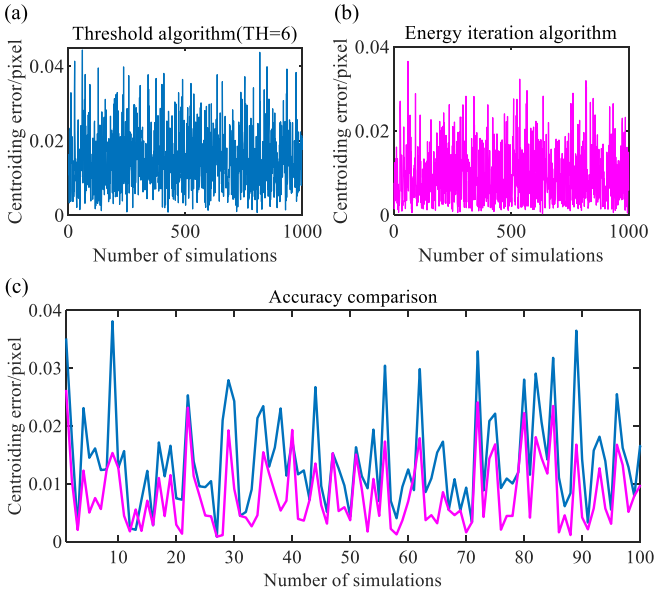

Fig. 9. (a) Traditional threshold algorithm. (b) EIWA algorithm. (c) Monte Carlo simulation comparison between (a) and (b).

Based on the above centering algorithm, the position of the centroid is measured by the continuous movement of subpixels $\tilde{x}_{k1}, \tilde{x}_{k2}, \ldots \tilde{x}_{kn} (\tilde{x}_{km+1} - \tilde{x}_{km} < 1$ pixel). The centroiding error curve is $\tilde{s}(x)$. Then, the system error curve is obtained by interpolation $\tilde{\delta}_s$. Finally, the centering curve is calculated as $\hat{s}(x)$ [40]

$$\tilde{\delta}_s(x_u) = \tilde{x}_c + \frac{x_u - x_c}{x_{c+1} - x_c}(\tilde{x}_{c+1} - \tilde{x}_c), \ (\tilde{x}_c < x_u < \tilde{x}_{c+1}). \tag{50}$$

Then, the centroiding curve can be obtained as

$$\hat{s}(x) = \tilde{s}(x) - \tilde{\delta}_c(x). \tag{51}$$

According to the previous simulation analysis, for the embodiment of the final centroiding accuracy, a stable calibration correction of the system error is required. The relevant experimental verification is carried out in the subsequent sections [41]–[43].

D. Time Efficiency Analysis of EIWA Method

The spot target localization algorithm needs to have real-time characteristics to meet the satellite on-orbit attitude calculation. Therefore, the time efficiency of the proposed algorithm is of great importance.

According to the literature on related localization algorithms, the related time-efficient simulation analysis is more common and clear [44]–[46]. In this part, different algorithms are implemented in MATLAB in the Microsoft Windows environment on a Quad-Core 3.2-GHz PC. Each simulation performed included 1000 spot targets with random noise. The average running times of different algorithms are compared in Table I.

From the simulation results, it can be obtained that the processing time of EIWA method is about 7.5 times and the iterative weighted algorithm is 30.1 times more than the traditional algorithm. For the number of iterations, the

TABLE I

PROCESSING TIME AND ITERATION NUMBERS' COMPARISON

Centroiding method	Processing time/ms	Iteration numbers
Traditional threshold algorithm	11.7	/
Iterative weighted algorithm	352.3	17
Energy iteration algorithm	87.4	6

TABLE II

PARAMETERS OF EXPERIMENT MATERIALS

Parameter	value
Focal length	25mm
Field of view	15°×12°
Resolution	1280×1024
Pixel size	5.3μm
Exposure time	1~100ms
Star magnitude limit	5.5Mv
Turntable accuracy	<1" (3σ)

EIWA method can complete in less than six times, and an iterative weighted algorithm needs 17 times. This result is similar to the literature [47], and the number of iterations increases significantly in the case of low SNR and complex spot target morphology. Because iterative algorithm requires fitting iterations to the morphology of the spot target, which requires a large number of fitting calculations.

From the EIWA algorithm principle, the main iteration is to traverse the pixel energy of the region and then use the traditional CG method to calculate centroids. For six iterations, it needs to calculate seven times centroids, which is the main time-consuming part. In the current APS CMOS star tracker, the CG method has already been modularly implemented by FPGA hardware and can realize the roll-up exposure pipeline fast calculation [48]. Therefore, the proposed algorithm can meet the real-time requirements in practical applications.

IV. SPOT TARGET LOCALIZATION ACCURACY EXPERIMENT

A. Laboratory Experiment

A laboratory experiment of spot target localization is carried out to verify the validity of the proposed algorithm. A star tracker is placed on a three-axis turntable and rotated by 1/15 pixel. Through image acquisition, the accuracy error curve is calibrated and measured. The schematic and parameters of the experimental equipment are shown in Table II and Fig. 10, respectively.

The following conclusions can be drawn by experimental comparison.

First, the traditional threshold connected domain centroid location method has poor static measurement stability. From the X- and Y-directions stability experiment shown in Fig. 11, since the calculated pixel is selected by a single threshold, the corresponding fluctuation in the centroiding calculation is caused by CMOS random noise.

The EIWA algorithm adopts an iterative method of finding minimal fluctuations in the local optimum centroiding, which ensures the stability of the prime extraction. Even if all

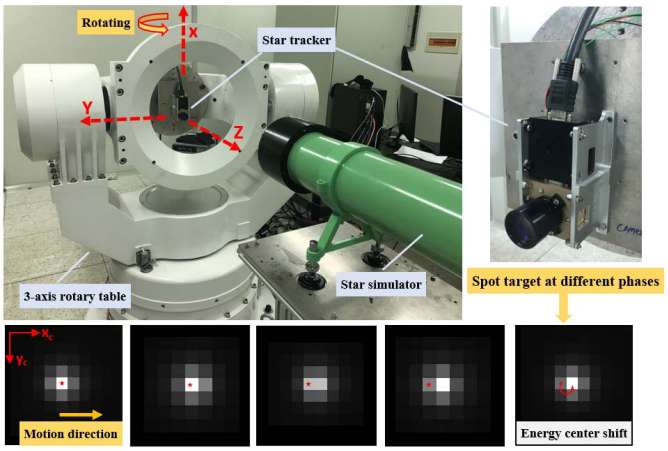

Fig. 10. Experiment of spot target localization.

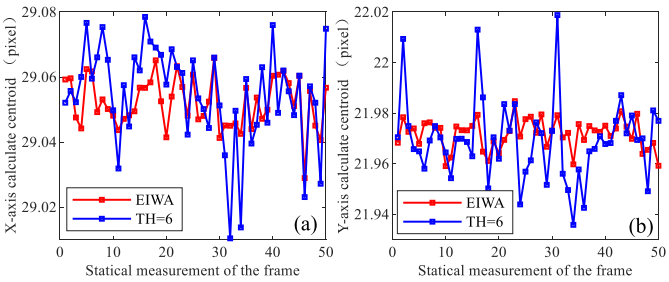

Fig. 11. Stability of threshold algorithm and energy iteration is compared in (a) X- and (b) Y-directions.

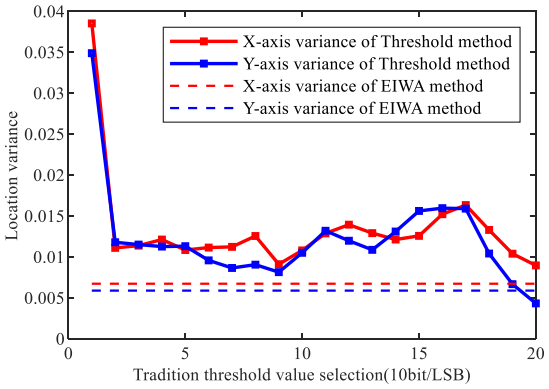

Fig. 12. Comparison of static stability between different threshold selection and energy iteration algorithm.

thresholds are traversed to select to calculate the stability, the EIWA algorithm still has better computational stability than the traditional method with lower centroiding error (shown in Fig. 12 and Table III).

The threshold selection scheme of the traditional threshold method is not unique. Pixels value that jumps around the threshold takes part in the calculation in different measurement frames. Although the pixel position with a low SNR affected by random noise can improve the positioning accuracy of the centroid at the expense of the pixel farther away from the centroid, the stability of static measurement fluctuates greatly.

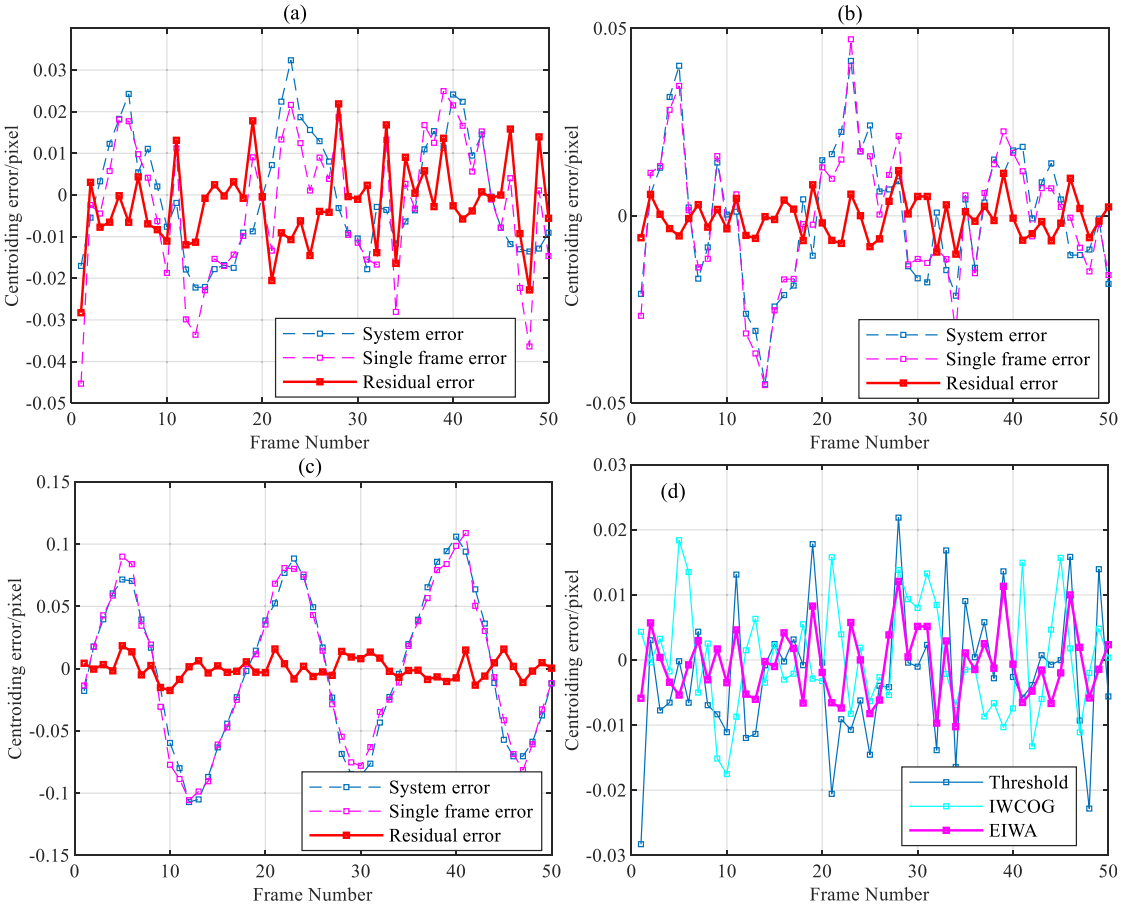

Fig. 13. Different methods: (a) traditional threshold, (b) energy iteration, and (c) iterative weighted. (d) Comparison of centroiding error.

All range static stability measurement is below the threshold value of the proposed energy iteration algorithm.

Second, the traditional threshold connected domain centroid localization method cannot accurately calibrate and correct the systematic errors δ_s in the centering process due to the influence of random noise.

Through calculation and comparison of experimental data, the calibration within the range of the full threshold value is not improved significantly. The proposed energy iteration method considers the influence of CMOS image detector noise and other random noises. The influence of spot target energy of different positions on the centroiding accuracy is analyzed. Also, iterate the suitable calculating window according to the degree of energy impact. Compared with the traditional threshold connected domain localization method, the proposed algorithm has higher stability of single measurement point and multiframe positioning and can effectively calibrate the centering system error caused by optical system design and pixel sampling. Although the IWCOG algorithm has a good model fitting ability for S-curve, its adaptation model receives a large impact from random noise. The proposed method can improve the positioning error from 1/100 magnitude to 1/1000 magnitude of centroiding accuracy (0.0106–0.0056 pixel, 47.2%, shown in Fig. 13 and Table IV).

The RMS error was used to evaluate the positioning accuracy between the traditional threshold method and the proposed iterative window algorithm. It is shown to be

$$\sigma_{\mathrm{RMS}} = \sqrt{\frac{\sum_{k=1}^{N} \delta_c^2(k)}{N}}. \tag{52}$$

B. Real Sky Experiment

In this section, a ground observation experiment of star tracker is designed to test the efficiency of the proposed algorithm. The experimental platform and the real sky observation are shown schematically in Fig. 14. The star tracker is mounted on the test platform that is fixed to the ground and controlled by turntable to observe suitable sky areas. The Earth's rotation is a very precise motion, so continuous real star spot target images can be obtained.

The experiment site is at the Xinglong observation station of National Astronomical Observatories of China (NAOC), East longitude 117°35.5′, North latitude 40°23′. During the observation period, weather is clear, no cloud cover, southwest wind less than level 3, and average temperature about 6°. Test tracking star information (shown in Fig. 15): StarID = 1651, declination = 41.23447°, right ascension = 76.62873°, star magnitude = 3.22 MV, total star energy = 398 LSB, and star area (7 pixel × 7 pixel). The pixel size is similar to the laboratory experiment. However, the SNR of the star is lower than that of the laboratory. According to the real sky

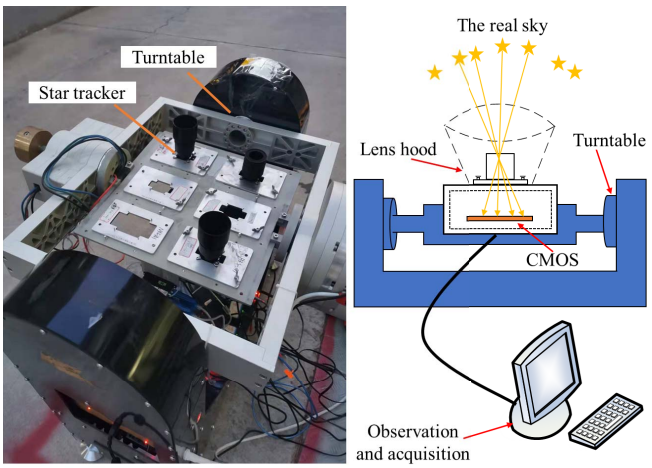

Fig. 14. Real sky experiment platform.

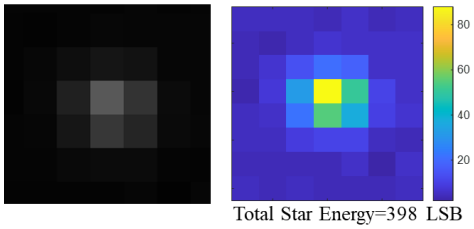

Fig. 15. Test tracking star energy distribution.

TABLE III
CENTROIDING STABILITY COMPARISON

Centroiding direction (RMS/pixel)	X	Y
Traditional threshold algorithm	0.0152	0.0160
Energy iteration algorithm	0.0077	0.0059
Contrast enhances	0.0075(49.3%)	0.0101(63.1%)

experiment, the image is clear. Also, the air disturbance and scattering have an effect on the centroiding. This part of the error is not analyzed precisely and eventually coupled in the error of centroiding together to be reduced by the proposed method.

The spot target centroids are calculated by using the proposed algorithm and the traditional threshold method. The 100 consecutive frames of centroiding error data are shown in Fig. 16. The traditional algorithm method has no significant periodic S-curve errors. While using the proposed algorithm to process, we can get the obvious systematic error with the pixel-by-pixel period. The shape of the systematic error and the standard S-curve error difference is large. Various factors cause this result, such as centroiding method error, star background removal, and atmospheric disturbances. Among them, the star image background of the real sky experiment is more complex than that of the laboratory experiment. After subtracting the background, it causes more star energy loss while causing systematic centroiding errors.

According to the previous error analysis, this kind of S-curve error can be further eliminated by means of a fitted calibration. A comparison of system residual results after

TABLE IV
CENTROIDING RMS ERROR COMPARISON REAL SKY EXPERIMENT

Centroiding method	RMS/pixel
Traditional threshold algorithm	0.0106
Iterative weighted algorithm	0.0085
Energy iteration algorithm	0.0056
Contrast enhances (RMS/pixel)	0.0050(47.2%)

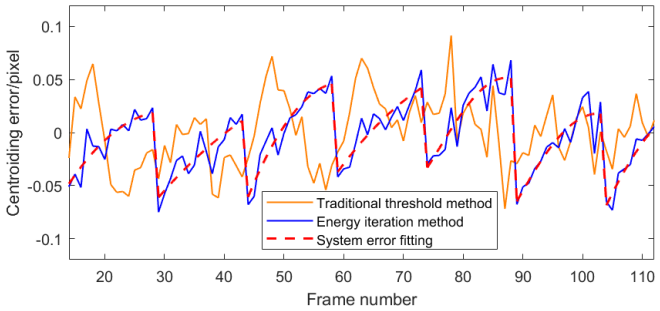

Fig. 16. Comparison of EIWA algorithm and traditional threshold method.

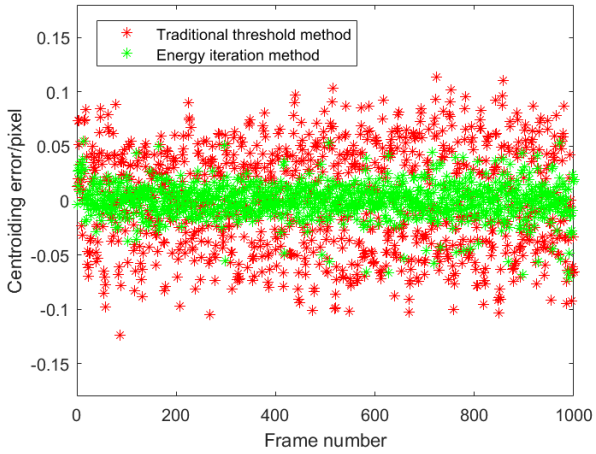

Fig. 17. Centroiding residual error results of 1000 consecutive frames.

TABLE V
CENTROIDING RMS ERROR COMPARISON

Centroiding method	RMS/pixel
Traditional threshold algorithm	0.0349
Energy iteration algorithm	0.0156
Contrast enhances (RMS/pixel)	0.0193(55.3%)

calibration correction of 1000 consecutive frames is shown in Fig. 17 and Table V. This algorithm can improve the centroiding accuracy from 0.0349 to 0.0156 pixels (55.3%).

Due to the low SNR ratio of the star spot target, we obtained in this experiment that the centroiding error is higher than the laboratory experimental situation. Also, the shape of the S-curve changes due to the influence of energy distribution.

The effectiveness of the proposed algorithm has been confirmed by testing with real star images. Its stability results in centroiding have been consistent with laboratory tests and simulation results. This algorithm feature can effectively calibrate the S-curve system error, which is important to further improve the centroiding accuracy.

V. Conclusion

The window-adaptive centroiding method based on the energy iteration algorithm successfully mitigates the impact of random noise of image detector on the centroiding. The method has better stability and time efficiency compared with other methods. Since the influence of noise position and size on the accuracy is considered, the model has a strong ability to adapt to different spot target morphology distributions. By experiment and simulation, we have compared the traditional threshold algorithm and improved iterative centroid algorithm. In the laboratory experiment, the proposed algorithm can improve centroid extraction accuracy from 0.0106 to 0.0056 pixels (1σ) (improvement of 47.2%). In the real sky experiment, the SNR of the star spot target is further reduced. It can improve from 0.0349 to 0.0156 pixels (1σ) (improvement of 55.3%). Both experiments verified the effectiveness of the proposed algorithm. In addition, it has a more stable accuracy of centroid extraction to fitting the systematic S-curve error effectively. The approach is an effective centroiding method for reducing the random noise without complicated iteration and fitting.

Acknowledgment

The authors acknowledge the support from TY-Space Technology (Beijing) Ltd., Beijing, China, for their cooperation in the experiment.

References

[1] J. Li and Y. Liu, "Modulation transfer function measurements using a learning approach from multiple diffractive grids for optical cameras," *IEEE Trans. Instrum. Meas.*, vol. 70, pp. 1–8, 2021.

[2] F. Jiancheng and N. Xiaolin, "Installation direction analysis of star sensors by hybrid condition number," *IEEE Trans. Instrum. Meas.*, vol. 58, no. 10, pp. 3576–3582, Oct. 2009.

[3] J. Li and Z. Liu, "Self-measurements of point-spread function for remote sensing optical imaging instruments," *IEEE Trans. Instrum. Meas.*, vol. 69, no. 6, pp. 3679–3686, Jun. 2020.

[4] E. Betzig "Imaging intracellular fluorescent proteins at nanometer resolution," *Science*, vol. 313, pp. 1643–1645, Sep. 2006.

[5] A. Yildiz *et al.*, "Myosin V walks hand-over-hand: Single fluorophore imaging with 1.5-nm localization," *Science*, vol. 5, pp. 155–157, Jan. 2008.

[6] M. Suliana *et al.*, "High-density mapping of single-molecule trajectories with photoactivated localization microscopy," *Methods. Nature.*, vol. 300, pp. 2061–2065, Jun. 2003.

[7] S. W. Hell, "Microscopy and its focal switch," *Nature Methods*, vol. 6, no. 1, pp. 24–32, Dec. 2008.

[8] R. W. Van, "SIRTF autonomous star tracker," *IR Space. Telescopes. Instrum.*, vol. 4850, pp. 108–121, Mar. 2003.

[9] U. Schmidt, "Astro APS—The next generation Hi-Rel star tracker based on active pixel sensor technology," in *Proc. AIAA Guid., Navigat., Control Conf. Exhib.*, Aug. 2005, p. 5925.

[10] V. B. Roei, "Flight performance of the spitzer space telescope AST-301 autonomous star tracker," *Guidance. Control.*, vol. 56, pp. 447–466, Sep. 2005.

[11] G. A. Beals, R. C. Crum, H. J. Dougherty, D. K. Hegel, J. L. Kelley, and J. J. Rodden, "Hubble space telescope precision pointing control system," *J. Guid., Control, Dyn.*, vol. 11, no. 2, pp. 119–123, Mar. 1988.

[12] E. Shalom, J. W. Alexander, and R. H. Stanton, "Acquisition and track algorithms for the ASTROS star tracker," *Advances. Astron. Sci.*, vol. 57, pp. 375–398, Jan. 1985.

[13] S. Du, M. Wang, X. Chen, S. Fang, and H. Su, "A high-accuracy extraction algorithm of planet centroid image in deep-space autonomous optical navigation," *J. Navigat.*, vol. 69, no. 4, pp. 828–844, Dec. 2015.

[14] A. Jorge and J. Arines, "Influence of thresholding on centroid statistics: Full analytical description," *Appl. Opt.*, vol. 43, no. 31, pp. 5796–5805, 2004.

[15] M. N. Sarvi, D. Abbasi-Moghadam, M. Abolghasemi, and H. Hoseini, "Design and implementation of a star-tracker for LEO satellite," *Optik*, vol. 208, Apr. 2020, Art. no. 164343.

[16] P. Jerram and K. Stefanov, "CMOS and CCD image sensors for space applications," in *High Performance Silicon Imaging*. Sawston, U.K.: Woodhead Publishing, 2020, pp. 255–287.

[17] W. Xu, Q. Li, H.-J. Feng, Z.-H. Xu, and Y.-T. Chen, "A novel star image thresholding method for effective segmentation and centroid statistics," *Optik*, vol. 124, no. 20, pp. 4673–4677, 2013.

[18] H. Poladyan, O, Bubon, and A. Teymurazyan, "Gaussian position-weighted center of gravity algorithm for multiplexed readout," *Phys. Med. Biol.*, vol. 65, no. 16, Aug. 2020, Art. no. 165003.

[19] A. Vyas, M. B. Roopashree, and R. P. Budihala, "Improved iteratively weighted centroiding for accurate spot detection in laser guide star based Shack Hartmann sensor," *Proc. SPIE*, vol. 7588, Feb. 2010, Art. no. 758806.

[20] L. Andrew and M. C. Polo, "Real-time algorithms implemented in hardware for centroiding on a Shack–Hartmann sensor," in *Proc. Adapt. Opt., Anal., Methods Syst.*, vol. 2, Jun. 2015, p. AOW3F-2.

[21] K. Fanpeng, M. C. Polo, and A. Lambert, "Centroid estimation for a Shack-Hartmann wavefront sensor based on stream processing," *Appl. Opt.*, vol. 56, no. 23, pp. 6466–6475, 2017.

[22] R. Jiang, X. Wang, and L. Zhang, "Localization algorithm based on iterative centroid estimation for wireless sensor networks," *Math. Problems Eng.*, vol. 2018, pp. 1–11, Oct. 2018.

[23] S. Thomas, T. Fusco, A. Tokovinin, M. Nicolle, V. Michau, and G. Rousset, "Comparison of centroid computation algorithms in a Shack-Hartmann sensor," *Monthly Notices Roy. Astronomical Soc.*, vol. 371, no. 1, pp. 323–336, Aug. 2006.

[24] T. Sun *et al.*, "Centroid determination based on energy flow information for moving dim point targets," *Acta Astronautica*, vol. 192, pp. 424–433, Mar. 2022.

[25] X. Wan, G. Wang, X. Wei, J. Li, and G. Zhang, "ODCC: A dynamic star spots extraction method for star sensors," *IEEE Trans. Instrum. Meas.*, vol. 70, pp. 1–14, 2021.

[26] Y. Zhang, J. Jiang, G. Zhang, and Y. Lu, "Accurate and robust synchronous extraction algorithm for star centroid and nearby celestial body edge," *IEEE Access*, vol. 7, pp. 126742–126752, 2019.

[27] M. Lelek *et al.*, "Single-molecule localization microscopy," *Nat. Rev. Methods Primers*, vol. 1, p. 40, Jan. 2021.

[28] D. Harshil, B. Theodore, and T. Abbie, "Wavefront reconstruction for noisy Shack–Hartmann wavefront sensors using deep learning," in *Propagation Through and Characterization of Atmospheric and Oceanic Phenomena*. Washington, DC, USA: Optical Society of America, Jul. 2021.

[29] P. Wei, X. Li, X. Luo, and J. Li, "Analysis of the wavefront reconstruction error of the spot location algorithms for the Shack–Hartmann wavefront sensor," *Opt. Eng.*, vol. 59, no. 4, Apr. 2020, Art. no. 043103.

[30] D. Rijlaarsdam, H. Yous, J. Byrne, D. Oddenino, G. Furano, and D. Moloney, "Efficient star identification using a neural network," *Sensors*, vol. 20, no. 13, p. 3684, Jun. 2020.

[31] G. Rufino and D. Accardo, "Enhancement of the centroiding algorithm for star tracker measure refinement," *Acta Astronautica*, vol. 53, pp. 135–147, Jul. 2003.

[32] J. Anderson and I. R. King, "Toward high-precision astrometry with WFPC2. I. Deriving an accurate point-spread function," *Publications Astronomical Soc. Pacific.*, vol. 112, p. 1360, Oct. 2000.

[33] X. Meng, Y. Wu, M. Wang, and H. Cheng, "Research on the accuracy evaluation method of ePSF model reconstruction," in *Proc. IEEE 6th Int. Conf. Comput. Commun. (ICCC)*, Dec. 2020, pp. 1573–1577.

[34] B. F. Alexander and K. C. Ng, "Elimination of systematic error in subpixel accuracy centroid estimation," *Opt. Eng.*, vol. 30, pp. 1320–1331, 1991.

[35] X. Wei, J. Xu, J. Li, J. Yan, and G. Zhang, "S-curve centroiding error correction for star sensor," *Acta Astronautica*, vol. 99, pp. 231–241, Jun. 2014.

[36] S. Zhang *et al.*, "Novel approach to improve the attitude update rate of a star tracker," *Opt. Exp.*, vol. 26, no. 5, pp. 5164–5181, Jun. 2018.

[37] M. Fiuzy, M. Hashemi, and S. K. M. Mashhadi, "A novel fixed pattern noise reduction algorithm in CMOS detector for LEO satellite application," in *Proc. 4th Int. Conf. Control, Instrum., Autom. (ICCIA)*, Jan. 2016, pp. 419–424.

[38] J. Zapata-Pérez, G. Doménech-Asensi, R. Ruiz-Merino, J. J. Martínez-Álvarez, J. Fernández-Berni, and R. Carmona-Galán, "Fixed pattern noise analysis for feature descriptors in CMOS APS images," *Sens. Imag.*, vol. 21, no. 1, pp. 1–24, Mar. 2020.

[39] M. Asadnezhad, A. Eslamimajd, and H. Hajghassem, "Optical system design of star sensor and stray light analysis," *J. Eur. Opt. Soc.-Rapid Publications*, vol. 14, no. 1, pp. 1–11, Mar. 2018.
[40] S. D. Waele and P. M. T. Broersen, "Error measures for resampled irregular data," *IEEE Trans. Instrum. Meas.*, vol. 49, no. 2, pp. 216–222, Apr. 2000.
[41] H. P. Zhang *et al.*, "Star detection and accurate centroiding for the geosynchronous interferometric infrared sounder of Fengyun-4A," *IEEE Access*, vol. 7, pp. 18510–18520, 2019.
[42] H. Jia, J. Yang, and X. Li, "Minimum variance unbiased subpixel centroid estimation of point image limited by photon shot noise," *J. Opt. Soc. Amer. A, Opt. Image Sci.*, vol. 27, no. 9, pp. 2038–2045, 2010.
[43] T. Sun, F. Xing, Z. You, and M. Wei, "Motion-blurred star acquisition method of the star tracker under high dynamic conditions," *Opt. Exp.*, vol. 21, no. 17, pp. 20096–20110, 2013.
[44] J. Jiang, J. N. Huang, and G. J. Zhang, "An accelerated motion blurred star restoration based on single image," *IEEE Sensors J.*, vol. 17, no. 5, pp. 1306–1315, Mar. 2017.
[45] J. Li, X. Wei, and G. Zhang, "Iterative algorithm for autonomous star identification," *IEEE Trans. Aerosp. Electron. Syst.*, vol. 51, no. 1, pp. 536–547, Jan. 2015.
[46] Y. Zhao, X. Wei, J. Li, and G. Wang, "Star identification algorithm based on K–L transformation and star walk formation," *IEEE Sensors J.*, vol. 16, no. 13, pp. 5202–5210, Jul. 2016.
[47] K. Baker and M. Moallem, "Iteratively weighted centroiding for Shack-Hartmann wave-front sensors," *Opt. Exp.*, vol. 15, no. 8, pp. 5147–5159, 2007.
[48] S. Zhang, F. Xing, T. Sun, Z. You, and M. Wei, "Novel approach to improve the attitude update rate of a star tracker," *Opt. Exp.*, vol. 26, no. 5, pp. 5164–5181, 2018.

Jingyu Bao was born in 1992. He received the B.S. degree in control technology from the School of Automation, Beijing Institute of Technology, Beijing, China, in 2014. He is currently pursuing the Ph.D. degree with the Department of Precision Instrument, Tsinghua University, Beijing.

His research focuses on high-precision space optical instruments.

Haiyang Zhan was born in 1996. He received the B.S. degree in automation from the Beijing Institute of Technology, Beijing, China, in 1997. He is currently pursuing the Ph.D. degree with the Department of Precision Instrument, Tsinghua University, Beijing.

His research focuses on high-precision optical measurements.

Ting Sun received the B.S. degree from Tianjin University, Tianjin, China, in 2009, and the Ph.D. degree in instrument science and technology from Tsinghua University, Beijing, China, in 2014.

Since 2016, she has been an Associate Professor with Beijing Information Science and Technology University, Beijing. Her main research interests include instrument technology, photoelectric measurement, and multisource information fusion.

Sheng Fu was born in 1994. He received the B.S. degree in measurement and control technology and instrument from Tianjin University, Tianjin, China, in 1997. He is currently pursuing the Ph.D. degree with the Department of Precision Instrument, Tsinghua University, Beijing, China.

His research focuses on optical system optimization and testing methods.

Fei Xing received the B.S. degree in mechanical engineering degree from Tongji University, Shanghai, China, in 2002, and the Ph.D. degree from Tsinghua University, Beijing, China, in 2006.

After graduation, he joined the Department of Precision Instrument, Tsinghua University, as an Assistant Researcher. He became a Professor in 2021. He was a Yangtze River Scholar Award Program Professor in 2020. He has published more than 70 articles. His main research interest includes micro-miniature high-precision attitude measurement sensor technology.

Zheng You received the B.S., M.S., and Ph.D. degrees from the Huazhong University of Science and Technology, Wuhan, China, in 1985, 1987, and 1990, respectively.

After graduation, he joined the Department of Precision Instrument, Tsinghua University, Beijing, China, as an Assistant Professor. He became an Associate Professor in 1992 and a Full Professor in 1994. In 2015, he was the Vice President of Tsinghua University. He was a Yangtze River Scholar Award Program Professor in 2001, and an Academician by the Chinese Academy of Engineering in 2013. He has published more than 400 articles. His main research interests include micro-nano technology and micro-nano satellite technology.